Journal of Applied Mechanics and Technical Physics, Vol. 48, No. 1, pp. 44–54, 2007

INTERACTION OF A CIRCULAR TURBULENT JET WITH A FLAT TARGET

K. N. Volkov

UDC 532.529:536.24

Large eddy simulations are performed for an unsteady flow and heat transfer in the region of interaction of a circular turbulent jet with a normally positioned flat obstacle (target). Space-filtered Navier–Stokes equations are closed by the RNG *model of eddy viscosity, which takes into account the curvature of streamlines in the region of flow turning. The computations are performed for different dimensionless distances between the nozzle exit and the target and for different Reynolds numbers. The dependence between the Nusselt number distribution over the target surface and the vortex structure of the jet is analyzed. The local and integral characteristics of the flow are compared with the data of a physical experiment.*

Key words: *turbulence, large eddy simulation, jet, target, heat transfer.*

Introduction. The study of the flow structure and heat transfer due to jet–target interaction is necessary to develop resource-saving technologies, which, in particular, include application of protective and reinforcing powder coatings. In these applications, intensification of the transport properties of the medium and the level of heat loads on the target are largely caused by the turbulent structure of the jet flow.

The flow structure and heat transfer in the jet–target interaction region are affected by the dimensionless distance between the nozzle exit and the target, conditions of jet exhaustion from the nozzle (Reynolds number and degree of turbulence), angle of impingement onto the target, etc.

In the case of the normal impact of the jet onto the target, the overall flow region can be divided into several subregions (Fig. 1). In the free jet flow region $r/D < 1$ (region I), the source of turbulence is the mixing layer separating the potential core of the flow (region V) with a constant axial velocity of the jet and the quiescent ambient fluid (region VI). If the distance between the nozzle exit and the target is small, no significant mixing of the jet with the ambient fluid occurs. The velocity at the jet axis remains unchanged at a distance from the nozzle exit $x/H = 0.4$. The turbulence intensity increases approximately by 5%, as compared with its value at the nozzle exit. In the region of flow deceleration $1 < r/D < 2$ (region II), the jet velocity on the wall vanishes, and the streamlines are substantially curved in the region of flow turning ($r/D \approx 1$). In terms of the x coordinate, the region of flow deceleration extends to a cross section located at a distance $x/H = 0.25$ from the target surface. For $H/D = 8$, the turbulence intensity in the vicinity of the target is approximately 25% higher than its value at the nozzle exit. For $H/D = 2$, the maximum of turbulent viscosity is located at the point $x/H = 0.18$ for $\mathrm{Re} = 2.3 \cdot 10^4$ and at the point $x/H = 0.12$ for $\mathrm{Re} = 7 \cdot 10^4$ (Re is the Reynolds number).

The effect of streamline curvature is responsible for flow stabilization and for the decrease in turbulent kinetic energy. The shear layer formed owing to jet mixing with the ambient fluid reaches the wall when it still has a rather high level of turbulence. The level of fluctuations of normal velocity is higher than the level of fluctuations of tangential velocity. The linear scale of turbulence depends on the flow history determined by jet-exhaustion conditions.

In the near-wall region $r/D > 2$ (region III), shear stresses start dominating over normal stresses.

Propagating along the target, the jet loses some momentum, and the boundary-layer thickness increases. In region IV, flow separation occurs, and large eddies are broken into a number of secondary vortices.

University of Surrey, Guildford, UK; k.volkov@surrey.ac.uk. Translated from Prikladnaya Mekhanika i Tekhnicheskaya Fizika, Vol. 48, No. 1, pp. 55–67, January–February, 2007. Original article submitted September 29, 2005; revision submitted January 23, 2006.

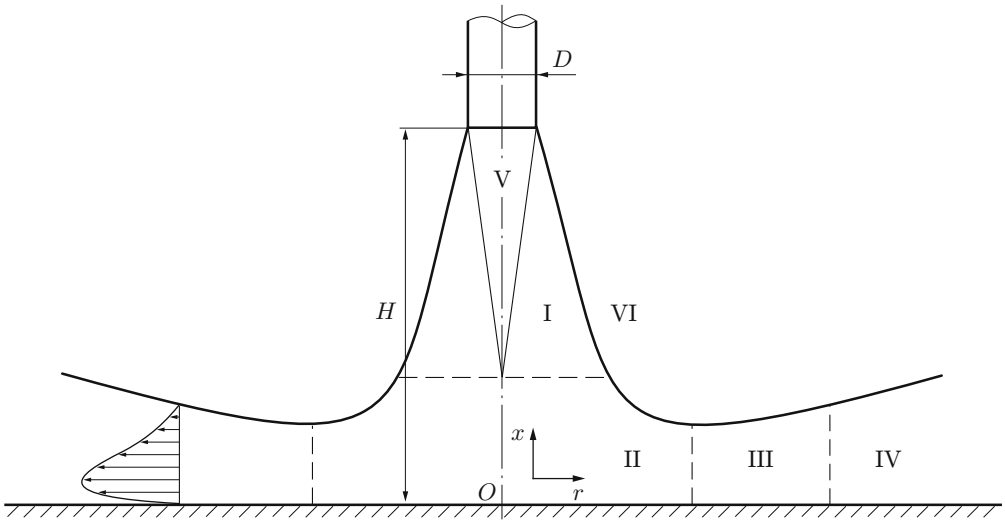

Fig. 1. Typical flow regions: free jet flow (I), flow-deceleration region (II), near-wall region (III), flow-separation region (IV), jet core (V), and ambient medium (VI).

Experimental studies [1, 2] were performed for Reynolds numbers $\mathrm{Re} = (2.3\text{–}7.0) \cdot 10^4$ and distances between the nozzle exit and the target $H/D = 2\text{–}10$. A detailed description of test conditions and results can be found in the ERCOFTAC database (`www.ercoftac.mech.surrey.ac.uk`). Under the same conditions, the data on heat transfer differ by 20–25%, which is caused by the difference in jet-exhaustion conditions [3]. The local characteristics of the flow (distributions of shear stresses over the target surface) are described in [4, 5].

For $H/D \leqslant 2$, the friction and heat flux at the stagnation point are estimated with the use of the exact solution for a laminar boundary layer [6]. With increasing distance between the nozzle exit and the target, the effect of the mixing layer starts to interfere, and the heat-transfer data deviate from the exact solution.

The main specific feature of free shear flows is the presence of large-scale vortex structures (large eddies) in the mixing layer. The vortex structures exert a significant effect on heat transfer in the jet–target interaction region. Heat-transfer characteristics fluctuate even at low Reynolds numbers ($\mathrm{Re} \approx 500$) [7]. Controlling of coherent structures by means of their amplification or breakdown offers wide possibilities for an effective impact on transport and heat-transfer processes.

The Nusselt number is maximum at the stagnation point (at $r = 0$), reaching the highest value for $H/D = 6\text{–}8$ [8], and its minimum value is observed in the region of flow turning (at $r/D \approx 1$). Further downstream (at $1 < r/D < 2$), the Nusselt number distributions at different times have a local maximum [1, 2]. At the same time, the time-averaged Nusselt number distribution has no local minimum [7].

Some experimental papers (see, e.g., [9, 10]) show that there is a local minimum of the heat-transfer coefficient and a ring hump with a maximum at $r/D \approx 0.5$ in the case of low values of H/D and moderate level of turbulence in the jet. For low values of H/D and sufficiently high values of Re, the secondary maximum of the heat-transfer coefficient is also observed in time-averaged distributions (for $r/D \approx 1.5\text{–}2.0$).

There may be several reasons for the local maximum of the Nusselt number. In particular, it may be caused by the laminar–turbulent transition in the boundary layer and by an increase in the turbulent kinetic energy in the near-wall jet [3, 11]. As was suggested in [7], the changes in heat-transfer characteristics in the jet–target interaction region may be caused by generation of large-scale vortex structures.

The flow arising owing to jet–target interaction is normally described by Reynolds-averaged Navier–Stokes equations. The research performed revealed the bottlenecks of various turbulence models.

For high and low Reynolds numbers, k–ε models overpredict the turbulent kinetic energy approximately by 55%, which leads to an increase in the heat flux almost by 41%. The standard k–ε model also overestimates the degree of jet expansion, predicts a too rapid decrease in temperature along the axial coordinate, and underestimates the velocity near the wall and overestimates the velocity in the external part of the flow [8]. The use of turbulence models for low Reynolds numbers leads to significant overestimation of the heat flux toward the wall. As the distance between the nozzle exit and the target increases, the difference in results also increases [12].

The curvature of streamlines in the region of flow deceleration is taken into account and turbulence production is predicted more accurately with the use of the Kato–Launder correction. The equation for the turbulent kinetic energy is supplemented by additional source terms, which have, in particular, a differential form [8]. It is also proposed [13] to restrict the time scale of turbulence in the Kolmogorov–Prandtl formula for turbulent viscosity and in the equation for the dissipative function. These modifications, nevertheless, do not improve data on heat transfer, and the value of turbulence is greater than that in the experiment [1, 2]. The use of differential source terms stabilizes the iterative process and requires introduction of lower relaxation (presentation of the solution at each next iteration as a linear combination of solutions obtained at the previous and current iterations).

The wall-function method underpredicts the velocity at $0.5 < r/D < 2.5$, and its profile at $r/D > 1.5$ is too steep. At $H/D = 2$ and $\mathrm{Re} = 2 \cdot 10^4$, the predicted turbulent kinetic energy is higher than the real value almost by a factor of 9 [14]. The accuracy of calculating the heat-transfer characteristics is improved by solving simplified equations for the turbulent kinetic energy and its dissipation rate in a near-wall reference volume [15].

Among two-parameter turbulence models, the most accurate results are provided by hybrid models, such as the two-layer $(k$–$\varepsilon)/(k$–$l)$ model and Menter's SST model [16].

The results of heat-transfer computations on the basis of nonlinear models of turbulent viscosity are 10% higher than the corresponding experimental values [8]. Moreover, nonlinear models overpredict turbulent stresses for $1.0 < r/D < 2.5$ and underpredict them for $r/D > 2.5$.

Fairly accurate results can be obtained with the use of multiparametric turbulence models, such as the k–ε–f_μ model and the v^2–f model [11].

Most researches dealt with time-averaged characteristics of the flow. Numerical computations based on solving the Reynolds equations do not allow studying the generation of large-scale vortex structures in the region of jet–target interaction.

Direct numerical simulation of jet–target interaction is restricted to low Reynolds numbers ($\mathrm{Re} < 5 \cdot 10^3$), and the computations are performed in a planar or axisymmetric formulation [7] (direct numerical simulation implies a three-dimensional problem).

Large eddy simulation (LES) involves testing of subgrid-scale models and finite-difference schemes and analysis of other issues of numerical implementation [17, 18]; therefore, many computations are performed in an axisymmetric formulation for an incompressible fluid. Olisson and Fuchs [18] used a dynamic model of subgrid-scale viscosity and a modification of the model of similar scales; they considered the mesh dependence of the solution (the computations were performed at $\mathrm{Re} = 10^4$ and $H/D = 4$). The computed results confirm the existence of secondary vortices in the near-wall region and their relation to the primary vortex formed in the mixing layer of the free jet with the quiescent ambient fluid. The primary vortex near the wall has a helical shape. The model yields more accurate results on a fine grid, and the difference in data on turbulence intensity obtained by using different subgrid-scale models is less than 10%.

The vortex structure of the flow and its influence on the characteristics of unsteady heat transfer in the jet–target interaction region have not been adequately studied and require further research.

The present paper describes the large eddy simulation for a circular turbulent jet interacting with a flat target and impinging normal onto the latter. In contrast to previous research, the condition of symmetry is not imposed (the stagnation point is not fixed in space). The vortex structure of the jet that is not perturbed by external sources is considered. The computations involve space-filtered Navier–Stokes equations closed by the model of eddy viscosity (with allowance for corrections for streamline curvature), which is constructed on the basis of the theory of renormalization groups (RNG model). The computations are performed for different dimensionless distances between the nozzle exit and the target and for different Reynolds numbers. The relation between the Nusselt number distribution over the target surface and intensity and position of vortex structures is analyzed.

Governing Equations. We consider an ambient turbulent jet interacting with a flat target normal to the latter. The origin is located at the point of intersection of the nozzle centerline with the target. The x coordinate is counted in the direction opposite to jet propagation.

In the Cartesian coordinate system (x, y, z), the unsteady flow of a viscous compressible gas is described by the following equation written for space-filtered quantities:

$$\frac{\partial \boldsymbol{Q}}{\partial t} + \frac{\partial \boldsymbol{F}}{\partial x} + \frac{\partial \boldsymbol{G}}{\partial y} + \frac{\partial \boldsymbol{H}}{\partial z} = 0. \tag{1}$$

Equation (1) is supplemented by the equation of state for a perfect gas:

$$p = (\gamma - 1)\rho[e - (u^2 + v^2 + w^2)/2].$$

The vector of conservative variables $\boldsymbol{Q}$ and the flux vectors $\boldsymbol{F}$, $\boldsymbol{G}$, and $\boldsymbol{H}$ have the following form:

$$\boldsymbol{Q} = \begin{pmatrix} \rho \\ \rho u \\ \rho v \\ \rho w \\ \rho e \end{pmatrix}, \qquad \boldsymbol{F} = \begin{pmatrix} \rho u \\ \rho uu + p - \tau_{xx} \\ \rho uv - \tau_{xy} \\ \rho uw - \tau_{xz} \\ (\rho e + p)u - u\tau_{xx} - v\tau_{xy} - w\tau_{xz} + q_x \end{pmatrix},$$

$$\boldsymbol{G} = \begin{pmatrix} \rho v \\ \rho vu - \tau_{yx} \\ \rho vv + p - \tau_{yy} \\ \rho vw - \tau_{yz} \\ (\rho e + p)v - u\tau_{yx} - v\tau_{yy} - w\tau_{yz} + q_y \end{pmatrix},$$

$$\boldsymbol{H} = \begin{pmatrix} \rho w \\ \rho wu - \tau_{zx} \\ \rho wv - \tau_{zy} \\ \rho ww + p - \tau_{zz} \\ (\rho e + p)w - u\tau_{zx} - v\tau_{zy} - w\tau_{zz} + q_z \end{pmatrix}.$$

The components of the viscous stress tensor and the components of the heat-flux vector are found from the relations

$$\tau_{ij} = \mu_{\text{eff}}\Big(\frac{\partial v_i}{\partial x_j} + \frac{\partial v_j}{\partial x_i} - \frac{2}{3}\,\frac{\partial v_k}{\partial x_k}\delta_{ij}\Big), \qquad q_i = -\lambda_{\text{eff}}\,\frac{\partial T}{\partial x_i},$$

where t is the time, ρ is the density, u, v, and w are the velocity components in the coordinate directions x, y, and z, respectively, p is the pressure, e is the total energy of a mass unit, T is the temperature, and γ is the ratio of specific heats.

Equation (1) formally coincides with unsteady Reynolds equations. The effective viscosity μ_{eff} is calculated as the sum of molecular viscosity μ and subgrid-scale turbulent viscosity μ_{sgs}, and the effective thermal conductivity λ_{eff} is expressed in terms of viscosity and the Prandtl number:

$$\mu_{\text{eff}} = \mu + \mu_{\text{sgs}}, \qquad \lambda_{\text{eff}} = c_p(\mu/\text{Pr} + \mu_{\text{sgs}}/\text{Pr}_{\text{sgs}}).$$

Here c_p is the specific heat at constant pressure (for air, $\text{Pr} = 0.72$ and $\text{Pr}_{\text{sgs}} = 0.9$).

Molecular viscosity is calculated by Sutherland's formula

$$\frac{\mu}{\mu_*} = \Big(\frac{T}{T_*}\Big)^{3/2}\frac{T_* + S_0}{T + S_0},$$

where $\mu_* = 1.68 \cdot 10^{-5}$ kg/(m $\cdot$ sec), $T_* = 273$ K, and $S_0 = 110.5$ K for air.

Subgrid-Scale Model. As a subgrid-scale model of viscosity, we use the RNG model, which is rather simple and efficient from the computational viewpoint but, in contrast to the Smagorinsky model, correctly predicts the behavior of subgrid-scale viscosity in the laminar flow region without any additional modifications ($\mu_{\text{sgs}} \to 0$ as $\text{Re} \ll 1$).

The calculation of effective viscosity $\mu_{\text{eff}} = \mu + \mu_{\text{sgs}}$ in the RNG model reduces to solving the nonlinear equation [19, 20]

$$\mu_{\text{eff}} = \mu[1 + H(X - C)]^{1/3}, \qquad X = 2A\Big(\frac{\Delta}{2\pi}\Big)^4\frac{\mu_{\text{sgs}}}{\mu^3}\,|S|^2, \tag{2}$$

where $H(X)$ is the Heaviside function, Δ is the filter width, $A = 0.12$, and $C = 75$.

In a strongly turbulent flow region, $\mu \ll \mu_{\text{sgs}}$, and hence, $\mu_{\text{eff}} \simeq \mu_{\text{sgs}}$. In this case, we have $X \gg C$, and relation (2) obtained from the RNG theory yields the Smagorinsky formula, which has a slightly different value of the constant factor. In a weakly turbulent region, the argument of the Heaviside function becomes negative; hence we have $\mu_{\text{eff}} \simeq \mu$.

To take into account the effects caused by streamline curvature, we multiple the subgrid-scale viscosity by a damping function depending on the Richardson number [21]:

$$f(\mathrm{Ri}_{\mathrm{sgs}}) = (1 - \alpha\,\mathrm{Ri}_{\mathrm{sgs}})^{1/2}.$$

Here $\alpha \approx 0.1$. The Richardson number is found by the formula

$$\mathrm{Ri}_{\mathrm{sgs}} = \frac{|\Omega|}{|S|}\Big(1 + \frac{|\Omega|}{|S|}\Big), \qquad |S| = (2S_{ij}S_{ij})^{1/2}, \qquad |\Omega| = (2\Omega_{ij}\Omega_{ij})^{1/2}.$$

The dependence between the filter width Δ and the step of the difference grid is

$$\Delta = V^{1/3} = (\Delta x \Delta y \Delta z)^{1/3},$$

where V is the cell volume, and Δx, Δy, and Δz are the grid steps in the coordinate directions x, y, and z, respectively.

In the boundary layer, the grid step in the direction normal to the wall Δx is replaced by the quantity $\hat{\Delta} x$, and the filter width is found as

$$\Delta = (\hat{\Delta} x \Delta y \Delta z)^{1/3};$$

note that $\hat{\Delta} x = \Delta x$ near the wall and $\hat{\Delta} x = \bar{\Delta} x$ far from the wall (the value of Δx smoothly changes between the above-indicated values). The quantity $\bar{\Delta} x$ is the mean value of Δx in the near-wall region, and $\hat{\Delta} x$ is found by the formula

$$\hat{\Delta} x = [(1/\Delta x)^{\alpha} + (1/\bar{\Delta} x)^{\alpha}]^{-1/\alpha},$$

where $\alpha = 3$.

Initial and Boundary Conditions. The gas is assumed to be at rest at the initial time ($u = v = w = 0$, $p = 1.013 \cdot 10^5$ Pa, and $T = 288$ K). No-slip and no-penetration conditions are imposed on the target surface for the normal and tangential velocity, and the wall temperature is prescribed. Slip conditions are set on the upper boundary of the computational domain (except for the nozzle exit). The boundaries are assumed to be adiabatic. The velocity profile set at the nozzle exit is [6]

$$u(x) = \frac{U_a}{3}\Big[1 + \tanh\Big(\frac{0.5 - |x|}{2\delta}\Big)\Big],$$

where U_a is the velocity at the jet centerline and δ is the momentum thickness ($\delta/D \approx 0.05$). The velocity profile is distorted by random perturbations (white noise). The root-mean-square values of perturbations are determined from the level of turbulence at the nozzle exit $\alpha k^{1/2}$, where $\alpha \approx 0.05$. The boundaries through which the gas leaves the computational domain are subjected to nonreflecting boundary conditions for velocity and temperature (conditions of convective transfer).

Numerical Method. Discretization of Eq. (1) is performed by the finite-volume method on an unstructured grid and by using difference schemes of high resolution in time and space [22].

The time discretization is performed by the five-step Runge–Kutta method

$$Q_i^{(m)} = Q_i^{(0)} - \alpha_m \Delta t_i R_i^{(m-1)} \qquad (m = 1, \ldots, 5).$$

Here $R_i^{(m-1)} = C_i(Q_i^{(m-1)}) - B_i^{(m-1)}$, $B_i^{(m-1)} = \beta_m D_i(Q_i^{(m-1)}) + (1 - \beta_m)B_i^{(m-2)}$, $C_i(Q_i^{(m-1)})$ is the contribution of convective terms, and $D_i(Q_i^{(m-1)})$ is the contribution of the source terms and physical and numerical dissipation. The coefficients α_m and β_m have the following values: $\alpha_1 = 1/4$, $\alpha_2 = 1/6$, $\alpha_3 = 3/8$, $\alpha_4 = 1/2$, and $\alpha_5 = 1$; $\beta_1 = 1$, $\beta_2 = 0$, $\beta_3 = 14/25$, $\beta_4 = 0$, and $\beta_5 = 11/25$.

A modified version of the MUSCL scheme is used for discretization of inviscid fluxes [23]:

$$F_{ij}^{\mathrm{inv}} = \{A_{ij}Q_j + A_{ij}Q_i - |A_{ij}|[(1 - \varphi)(\hat{L}_j^*(Q) - \hat{L}_i^*(Q))/3 + \varphi(Q_j - Q_i)]\}/2.$$

Here $\hat{L}^*(Q)$ is a modified pseudo-Laplacian. The relation between the finite differences of the second and fourth orders is established by the function

$$\varphi = \min\Big\{\varepsilon\Big|\frac{p_j - p_i}{p_j + p_i}\Big|^2, 1\Big\},$$

where $\varepsilon \approx 8$. The pseudo-Laplacian is the generalization of the central difference derivative to an unstructured grid:

$$L_i(Q) = \frac{1}{|E_i|} \sum_{j \in E_i} (Q_j - Q_i).$$

With such a definition, the scheme has no second-order accuracy on a nonuniform grid, and the pseudo-Laplacian is re-defined as

$$L_i^*(Q) = L_i(Q) - \nabla Q_i L_i(\boldsymbol{x}).$$

To ensure solution stability on a strongly extended grid, the modified pseudo-Laplacian is found from the relation

$$\hat{L}_i^*(Q) = \hat{L}_i(Q) - \nabla Q_i \, \hat{L}_i(\boldsymbol{x}), \qquad \hat{L}_i(Q) = \Big(\sum_{j \in E_i} \frac{1}{|\boldsymbol{x}_j - \boldsymbol{x}_i|} \Big)^{-1} \sum_{j \in E_i} \frac{Q_j - Q_i}{|\boldsymbol{x}_j - \boldsymbol{x}_i|}.$$

The expression for the gradient is obtained from the Green formula

$$(\nabla Q)_i = \frac{1}{V_i} \Big[\sum_{j \in E_i} \frac{1}{2} (Q_j - Q_i) \boldsymbol{n}_{ij} \Delta s_{ij} \Big].$$

Here E_i is the set of internal faces connected with the node i, $\boldsymbol{n}_{ij}$ is the external unit normal, which defines the orientation of the face (i, j), and Δs_{ij} is the area of the face connecting the nodes i and j.

Discretization of viscous fluxes is performed by centered difference formulas of the second order. The system of difference equations is solved by a multigrid method based on the scheme of complete approximation (a V-cycle and four grid levels are used). The sequence of nested grids is constructed by the method of collapsing edges [22]. The computational procedure is implemented as a computer code in the Fortran and C/C++ programming languages. Parallelization of the computational procedure is performed by a Message Passing Interface (MPI). The computations were performed on an IBM SP/1600 supercomputer with eServer pSeries 690 units on the basis of the Power 4+ processor (1.7 GHz and 6.8 Flops). The supercomputer center is based at Daresbury Laboratory, United Kingdom.

Computation Results. The computations were performed in the domain $[0, H] \times [-L_y, L_y] \times [-L_z, L_z]$, where $L_y = L_z = 10D$. The varied parameters were the distance between the nozzle exit and the target (H/D = 1–12) and the Reynolds number ($\mathrm{Re} < 10^5$). The other parameters of the problem had the following values: $D = 0.04$ m, flow temperature at the nozzle exit $T_a = 400$ K, temperature of the target (wall) $T_\mathrm{w} = 320$ K, and ambient pressure $p_\infty = 10^5$ Pa. The experiments were performed in air.

The potential core of the jet extends to a distance of the order of 4–8 jet diameters; therefore, some of the computations were performed for a completely developed turbulent flow, and some computations correspond to the case where the target is within the potential core of the jet. The computations were performed for both low Reynolds numbers ($\mathrm{Re} \approx 10^3$) where the laminar–turbulent transition does not play any significant role [3, 11] and high Reynolds numbers ($\mathrm{Re} \approx 10^5$).

For $H/D = 12$, we used a $240 \times 200 \times 200$ grid. As the distance between the nozzle exit and the target was changed, the number of grid nodes in the x direction was decreased in a manner that preserved an acceptable ratio of the lengths of the finite-volume faces. The grid was refined near the jet axis and near the target surface. The maximum step along the x coordinate was used near the nozzle exit ($\Delta x_{\max} = 0.18H$), and the minimum step was used near the plate surface ($\Delta x_{\min} = 0.0012H$), which corresponds to $\Delta x^+ \approx 0.16$. The minimum y and z steps near the jet centerline were $\Delta y_{\min} = \Delta z_{\min} = 0.0038H$. The time step was assumed to be $\Delta t = 1.2 \cdot 10^{-5}$ sec (with the Reynolds number being varied, the time step was estimated as $\Delta t \approx 10^{-3} D/U_a$). Up to 50,000 time steps were performed to obtain a statistically reliable averaged flow pattern.

The reference scales for variables with dimensions of length and velocity were the nozzle diameter D and the velocity at the jet centerline U_a, respectively. The dimensionless time was introduced as tU_a/D.

A cylindrical (x, r) coordinate system was used instead of the Cartesian coordinate system (x, y, z) for data processing. The time-averaged velocity component in the azimuthal direction equaled zero.

The shear layer of the jet contains large eddies in the form of toroidal axisymmetric vortices incipient at a certain distance from the nozzle exit (approximately 1–2 nozzle diameters) and propagating in the mixing layer in the downstream direction.

Generation of the primary vortex is associated with shear-layer instability of the Kelvin–Helmholtz instability type. The vorticity maximums and minimums roughly correspond to vortex centers. For low Reynolds numbers ($\mathrm{Re} \approx 10^3$), the jet is almost axisymmetric near the nozzle exit. As the distance from the nozzle exit and the

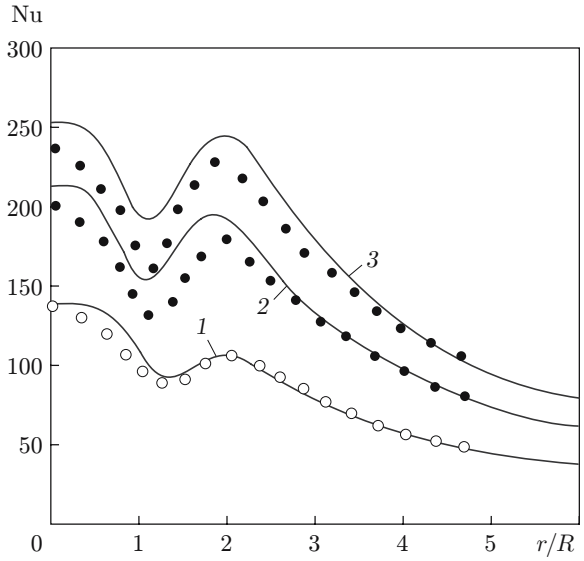

Fig. 2. Distribution of the Nusselt number over the target surface for $H/D = 2$: the solid curves are the computed results, and the points are the data of physical experiments [1, 2] (the open and filled points are the data of [1] and [2], respectively); the curves refer to $\mathrm{Re} = 2.3 \cdot 10^4$ (1), $5 \cdot 10^4$ (2), and $7 \cdot 10^4$ (3).

Reynolds number are increased (up to $\mathrm{Re} \approx 10^4$), a weak sinusoidal mode appears, and the stagnation point fluctuates around the geometric center of the target (point $r = 0$). A further increase in the Reynolds number makes the flow completely three-dimensional and turbulent ahead of the target.

The contours of the coherent structure are ellipses, which is indicative of anisotropy of turbulent fluctuations in the region with large-scale vortices present. This region is characterized by a nonzero skewness factor (third moment). Vortex breakdown begins in the region of vortex–target interaction, where the flow experiences the action of an adverse pressure gradient.

The velocity at the jet centerline decreases from U_a at the nozzle exit to zero on the target wall. For $H/D = 8$, the turbulence intensity at a distance from the nozzle exit equal to (3–4)D is 5% higher than its value at the nozzle exit, and the turbulence intensity near the target is 25% higher than its value at the nozzle exit.

The level of velocity fluctuations at the stagnation point remains unchanged as long as the target is in the potential core of the jet. The distribution of velocity fluctuations has a minimum at the stagnation point, and its maximum is located at a point where the shear layer reaches the surface. This position depends on the value of H/D.

The Nusselt number and the heat flux to the wall are found from the relations

$$\mathrm{Nu}(r) = \frac{q(r)D}{\lambda(T_\mathrm{w} - T_a)}, \qquad q(r) = \lambda\Big(\frac{dT}{dx}\Big)_\mathrm{w}.$$

Deviation of the Nusselt number from its mean value is calculated by the formula

$$\Delta\,\mathrm{Nu}_0 = \frac{\mathrm{Nu}_0 - \langle \mathrm{Nu}_0 \rangle}{\langle \mathrm{Nu}_0 \rangle}.$$

The broken brackets indicate time averaging; the subscript 0 refers to parameters at the stagnation point.

The computed distributions of the Nusselt numbers over the target surface are compared with the measured data for different Reynolds numbers in Fig. 2. The Nusselt number distribution has two peaks, one of them is at the stagnation point, and the position of the other maximum depends on the distance between the nozzle exit and the target. In the dependence $(r/D, \mathrm{Nu})$, the maximums of the Nusselt number corresponding to different values of H/D are located almost on one straight line (not shown in Fig. 2).

For low values of H/D, the Nusselt number at the stagnation point is adequately described by the dependence $\mathrm{Nu}_0 \sim \mathrm{Re}^{0.5}$, which follows from the solution for a laminar boundary layer in the vicinity of the stagnation point

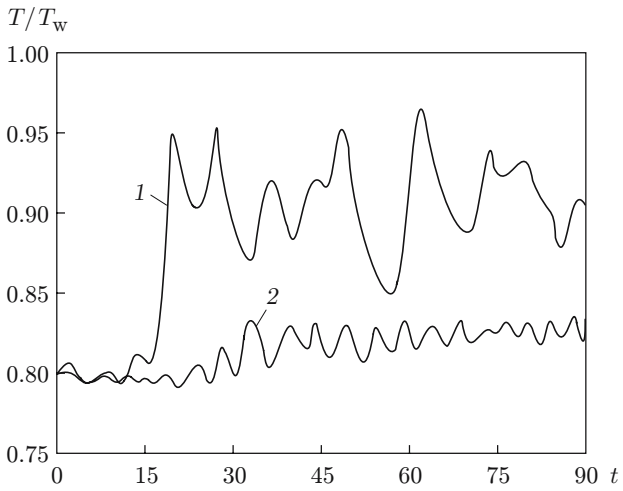

Fig. 3. Time evolution of temperature at a distance from the target surface $x/D = 0.02$ for $H/D = 10$, $\mathrm{Re} = 10^3$, and $r = 0$ (1) and $4H$ (2).

[6]. It should be noted that such a dependence is validated by measured data for rather high Reynolds numbers as well [3].

Because of generation of large eddies, the heat-transfer characteristics are time-dependent (Fig. 3). Temperature fluctuations begin at the moment when the primary vortex reaches the target (curve 1). It should be noted that this time is only weakly dependent on the Reynolds number. Temperature fluctuations downstream of the stagnation point (curve 2) are caused by the motion of the vortex structures in the direction parallel to the wall. The decrease in the amplitude of fluctuations is due to mixing of the near-wall jet with the ambient fluid.

Temperature fluctuations are not rigorously periodic, and their amplitude increases with increasing Reynolds number (at low Reynolds numbers, the intensity of the vortex structures is rather low, since viscous effects only weakly influence shear-layer instability). As the distance between the nozzle exit and the target decreases, the vortices do not have enough time to form completely, and the amplitude and frequency of temperature fluctuations become smaller.

The fluctuating component of the Nusselt number is commensurable with its mean value even at low Reynolds numbers (Nu_0' is approximately 40% of the mean Nusselt number $\langle \mathrm{Nu}_0 \rangle$ for $\mathrm{Re} \approx 500$); for $r = \pm 3D$, it is close to $\langle \mathrm{Nu}_0 \rangle$ (Figs. 4 and 5).

An increase in the Reynolds number leads to greater fluctuations of the Nusselt number at the stagnation point. For instance, the amplitude of fluctuations is 20% of the mean Nusselt number for $\mathrm{Re} = 5 \cdot 10^3$ and reaches 35% for $\mathrm{Re} = 2.5 \cdot 10^4$. The Strouhal number based on the velocity at the jet centerline and on the nozzle-exit diameter is $\mathrm{Sh} = 0.20$ and 0.32, respectively.

The minimum of the friction coefficient and the maximum of the Nusselt number are always located at the stagnation point, though their values change in time rather significantly (Figs. 6 and 7). The Nusselt number distribution along the wall at different times also has a local maximum, whereas the time-averaged Nusselt number changes monotonically along the wall.

It is rather difficult to compare the time evolution of computed and experimental distributions of local characteristics for flows without expressed external perturbations. Therefore, a comparison is performed for time-averaged values. Figure 6 shows the computed time-averaged skin-friction coefficient and the experimental data of [5].

For high values of r/D, the distribution of heat-transfer characteristics depends on the structure of secondary vortices arising owing to interaction of the primary vortex with the boundary layer of the near-wall jet. The unsteady character of this interaction and a change in the structure of the thermal boundary layer are responsible for a local maximum in the Nusselt number.

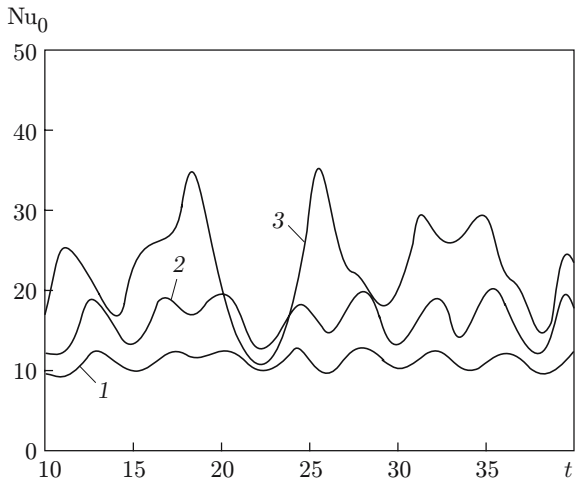

Fig. 4

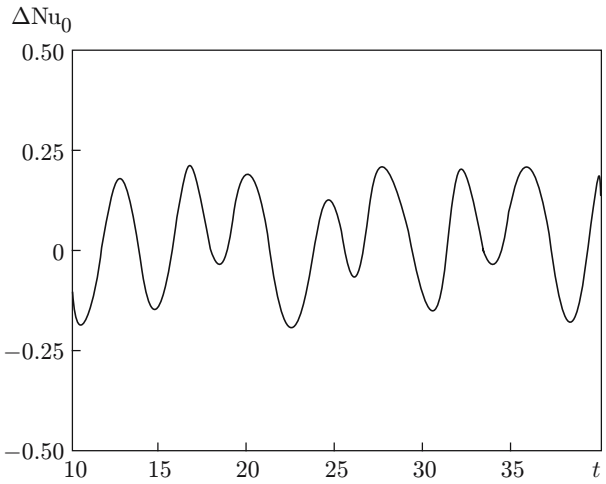

Fig. 5

Fig. 4. Nusselt number at the stagnation point versus time for $H/D = 5$ and $\mathrm{Re} = 300$ (1), 500 (2), and 1000 (3).

Fig. 5. Deviation of the Nusselt number from the mean value at the stagnation point versus time for $H/D = 5$ and $\mathrm{Re} = 500$.

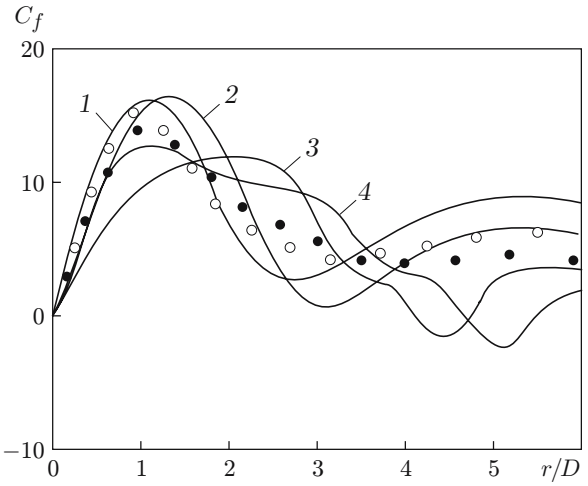

Fig. 6

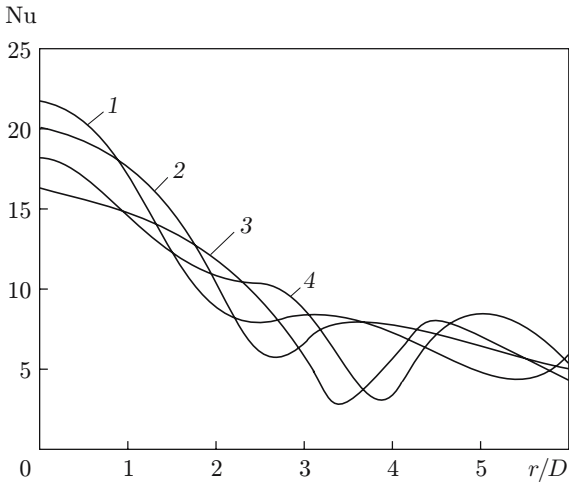

Fig. 7

Fig. 6. Distribution of the friction coefficient over the surface for $H/D = 5$, $\mathrm{Re} = 500$, and $t = 10$ (1), 20 (2), 30 (3), and 40 (4); the points show the distributions of the time-averaged friction coefficient (the filled and open points refer to the computed results and experimental data of [5]).

Fig. 7. Distribution of the Nusselt number over the surface for $H/D = 5$, $\mathrm{Re} = 500$, and $t = 10$ (1), 20 (2), 30 (3), and 40 (4).

For Re ≈ 500, the difference in the Nusselt number distributions along the wall on both sides of the stagnation point is 0.5%; for Re ≈ 10^3, it reaches 2%.

For low values of H/D, the Nusselt number fluctuations are insignificant. The length of the potential core increases with increasing Reynolds number. Therefore, the maximum in the Nusselt number appears at $H/D \approx 2$ for Re = 10^4 and is shifted toward higher values of H/D for Re = $2 \cdot 10^4$. At $H/D = 2.5$, the Nusselt number fluctuations increase from 6 to 27% of its mean value in the range H/D = 1–8.

Conclusions. Large eddy simulations are performed for an unsteady flow and heat transfer in the vicinity of interaction of a circular turbulent jet with a flat target for different dimensionless distances between the nozzle exit and the target and for different Reynolds numbers. The local and integral characteristics of the flow are compared with available numerical and experimental data. Large-scale vortex structures are found to exert a significant effect on skin-friction and heat-transfer characteristics. The distribution of the time-averaged Nusselt number over the target surface has two maximums, one of them is located at the stagnation point, and the position of the other maximum depends on the distance between the nozzle exit and the target.

Fluctuations of heat-transfer characteristics are not rigorously periodic, and their amplitude increases with increasing Reynolds number. More intense heat transfer is caused by extension of vortices in the direction parallel to the wall. Flow evolution under the action of an adverse pressure gradient and flow separation from the wall lead to formation of secondary vortices responsible for a local maximum of the Nusselt number.

REFERENCES

1. J. Baughn, A. Hechanova, and X. Yan, "An experimental study of entrainment effects on the heat transfer from a flat surface to a heated circular impinging jet," *J. Heat Transfer*, **113**, 1023–1025 (1991).
2. D. Cooper, D. Jackson, B. Launder, and G. Liao, "Impinging jet studies for turbulence model assessment. Flow-field experiments," *Int. J. Heat Mass Transfer*, **36**, No. 10, 2675–2684 (1993).
3. D. Lytle and B. Webb, "Air jet impingement heat transfer at low nozzle-plate spacings," *Int. J. Heat Mass Transfer*, **37**, No. 2, 1687–1697 (1994).
4. S. V. Alekseenko, V. V. Kulebyakin, D. M. Markovich, et al., "Local characteristics of an axisymmetric impinging jet," *Inzh.-Fiz. Zh.*, **69**, No. 4, 615–624 (1996).
5. D. J. Phares, G. T. Smedley, and R. C. Flagan, "The wall shear stress produced by the normal impingement of a jet on a flat surface," *J. Fluid Mech.*, **418**, 351–375 (2000).
6. G. Schlichting, *Boundary Layer Theory*, McGraw-Hill, New York (1968).
7. Y. M. Chung, K. H. Luo, and N. D. Sandham, "Numerical study of momentum and heat transfer in unsteady impinging jets," *Int. J. Heat Fluid Flow*, **23**, No. 5, 592–600 (2002).
8. T. J. Craft, H. Iacovides, and J. H. Yoon, "Progress in the use of non-linear two-equation models in the computation of convective heat-transfer in impinging and separated flows," *Flow, Turbulence Combust.*, **63**, Nos. 1/4, 59–80 (2000).
9. R. Gardon and J. Cobonpue, "Heat transfer between a flat plate and jets of air impinging on it," in: *International Development in Heat Transfer,* Proc. of the Int. Heat transfer Conf., ASME, New York (1961), pp. 454–460.
10. C. J. Hoogendoorn, "The effect of turbulence on heat transfer at stagnation point," *Int. J. Heat Mass Transfer*, **20**, No. 12, 1333–1338 (1977).
11. M. Behnia, S. Parneix, and P. A. Durbin, "Prediction of heat transfer in an axisymmetric turbulent jet impinging on a flat plate," *Int. J. Heat Mass Transfer*, **41**, No. 13, 1845–1855 (1998).
12. K. Heyerichs and A. Pollard, "Heat transfer in separated and impinging turbulent flows," *Int. J. Heat Mass Transfer*, **39**, No. 12, 2385–2400 (1996).
13. P. A. Durbin, "On the k–ε stagnation point anomaly," *Int. J. Heat Fluid Flow*, **17**, No. 1, 89, 90 (1996).
14. S. Ashforth-Frost and K. Jambunathan, "Numerical prediction of semi-confined jet impingement and comparison with experimental data," *Int. J. Numer. Methods Fluids*, **23**, No. 3, 295–306 (1996).
15. R. Amano and S. Sugiyama, "Investigation on turbulent heat transfer of an axisymmetric jet impinging on a flat plate," *Bull. JSME*, **28**, No. 235, 74–79 (1983).
16. W. Vieser, T. Esch, and F. Menter, "Heat transfer predictions using advanced two-equation turbulence models," Report No. CFX-VAL10/0602, CFX Validation, London (2002).

17. P. R. Voke and S. Gao, "Numerical study of heat transfer from an impinging jet," *Int. J. Heat Mass Transfer*, **41**, No. 5, 671–680 (1998).
18. M. Olisson and L. Fuchs, "Large eddy simulations of a forced semiconfined circular impinging jet," *Phys. Fluids*, **10**, No. 2, 476–486 (1998).
19. A. Yakhot, S. A. Orszag, V. Yakhot, and M. Israeli, "Renormalization group formulation of large-eddy simulation," *J. Sci. Comput.*, **1**, 1–51 (1986).
20. K. Horiuti, "Backward scatter of subgrid-scale energy in wall-bounded and free shear turbulence," *J. Phys. Soc. Jpn.*, **66**, No. 1, 91–107 (1997).
21. S. Shen, F. Ding, J. Han, et al., "Numerical modeling studies of wake vortices: real case simulation," AIAA Paper No. 99-0755 (1999).
22. K. N. Volkov, "Application of the control-volume method for the solution of problems in gas and fluid mechanics on unstructured grids," *Vychisl. Met. Program.*, **6**, No. 1, 43–60 (2005).
23. G. Zhou, L. Davidson, and E. Olsson, "Transonic inviscid/turbulent airfoil flow simulations using a pressure based method with high order schemes," *Lecture Notes Phys.*, No. 453, 372–377 (1995).